RSC Advances

PAPER

View Article Online
View Journal | View Issue

Check for updates

Cite this: *RSC Adv.*, 2022, **12**, 24980

3D printing lamellar $Ti_3C_2T_x$ MXene/graphene hybrid aerogels for enhanced electromagnetic interference shielding performance†

Tianxiang Hua,‡[ab] Hao Guo,‡[b] Jing Qin,[ab] Qixin Wu,[ab] Lingying Li[b] and Bo Qian*[ab]

Two-dimensional (2D) transition-metal carbides and nitrides (MXenes), especially $Ti_3C_2T_x$ nanosheets, offer high conductivities comparable to metal, and are very promising for fabricating high performance electromagnetic interference (EMI) shielding materials. Due to the weak gelation capability of MXenes, MXene/graphene hybrid aerogels were mostly studied. Among those studied, anisotropic hybrid aerogels showed excellent electrical properties in certain direction due to the intrinsic anisotropic properties of 2D materials. However, the present preparation methods for anisotropic hybrid aerogels lack freedom of geometry, and their electrical performances still have room for improvement. In this study, based on our previous work, the lamellar $Ti_3C_2T_x$ MXene/graphene hybrid aerogels generated by 3D printing with $Ti_3C_2T_x$ MXene/graphene oxide (GO) water–TBA dispersions demonstrated enhanced conductivity and electromagnetic interference (EMI) shielding performance. The addition of MXene deeply influenced the lamellar structure of the hybrid aerogels, and made the structure more ordered than that in the 3D printed lamellar graphene aerogels. The printed lamellar MXene/graphene hybrid aerogels achieved a maximum electrical conductivity of 1236 S m^{-1}. The highest EMI shielding efficiency (EMI SE) of the hybrid aerogels was up to 86.9 dB, while the absolute shielding effectiveness (SSE/*t*) was up to 25 078.1 dB cm^2 g^{-1} at 12.4 GHz. These values are higher than those of most reported anisotropic MXene-based nanocomposite aerogels.

Received 10th May 2022
Accepted 15th August 2022

DOI: 10.1039/d2ra02951k

rsc.li/rsc-advances

Open Access Article. Published on 01 September 2022. Downloaded on 4/29/2026 2:23:41 AM.
This article is licensed under a Creative Commons Attribution-NonCommercial 3.0 Unported Licence.

Introduction

The rapid development of information technology has accelerated the popularization of electronic equipment.[1] However, the EMI introduced by electronic equipment will not only cause the fault of the electronic equipment, but also impact human health and the environment.[2,3] Current EMI shielding materials mainly include metal materials (silver,[4] copper[5] and aluminum[6]), which have excellent EMI shielding properties.[7] However, they have obvious drawbacks: easy corrosion, high density, poor processability[8] and the secondary pollution caused by the reflection.[9] Therefore, researchers aim to develop multifunctional EMI shielding materials with ultralight weight, wide bandwidth, high flexibility and stability.[10]

2D Material-based aerogels are one of the most promising candidates to fulfill these requirements. Among them, MXene-based aerogels have attracted tremendous attention. As a new family of 2D transition metal carbides and nitrides,[11,12] MXenes, particularly $Ti_3C_2T_x$ nanosheets, are lightweight and have a high aspect ratio, hydrophilic surface, excellent mechanical and superb electrical properties.[10,13–15] In particular, the abundant termination functional groups on MXenes result in a high dipole polarization and interface polarization, which will raise considerable polarization loss, as well as EMI SE.[11,16]

Currently, considering the weak gelation capability of MXenes,[17] MXene/graphene hybrid aerogels have been mostly studied, and demonstrated high EMI shielding performances. Among these works, the aerogels with oriented structures strengthened the EMI shielding performances in the direction perpendicular to the orientation plane due to the intrinsic anisotropic properties of 2D materials. Zhao *et al.*[18] assembled $Ti_3C_2T_x$ sheets into a highly conductive, porous and 3D structure through GO-assisted hydrothermal assembly. The prepared 2 mm $Ti_3C_2T_x$MXene/rGO aerogels exhibited the highest EMI SE of 56.4 dB at 12.4 GHz. Liang *et al.*[19] used the wood-derived porous carbon (WPC) skeleton from natural wood as a template to construct ultralight 3D $Ti_3C_2T_x$ MXene/WPC composites, and the 3 mm samples exhibited the maximum EMI SE of 71.3 dB in the X-band. Sambyal *et al.*[2] prepared homogeneous and aligned 3D porous $Ti_3C_2T_x$MXene/carbon nanotube (CNT) hybrid aerogels through the bidirectional freeze-drying method, and the highest EMI SE of 103.9 dB was reached in the X-band of the 3 mm samples. Due to the simple

[a]*School of Nano-Tech and Nano-Bionics, University of Science and Technology of China, China. E-mail: bqian2010@sinano.ac.cn*

[b]*Suzhou Institute of Nano-Tech and Nano-Bionics, Chinese Academy of Sciences, China*

† Electronic supplementary information (ESI) available. See https://doi.org/10.1039/d2ra02951k

‡ These authors contributed equally to this work.

© 2022 The Author(s). Published by the Royal Society of Chemistry

Open Access Article. Published on 01 September 2022. Downloaded on 4/29/2026 2:23:41 AM.
This article is licensed under a Creative Commons Attribution-NonCommercial 3.0 Unported Licence.

operation, people prefer to use the bidirectional freezing method. However, this method lacks the freedom of geometry, and the electrical performances of the MXenes/graphene hybrid aerogels still have room for improvement.

3D Printing is an easy operation method with freedom of geometry. Our recent work on graphene aerogels prepared by a customized slit extrusion head has demonstrated great improvement of the EMI shielding performance.[20] Based on that result, in this paper, we applied the 3D printing method in the preparation of lamellar MXene/graphene hybrid aerogels to explore higher EMI SE and the MXene addition-related mechanisms.

By tuning the concentration of the $Ti_3C_2T_x$ MXene in the hybrid dispersions, the MXene/graphene hybrid aerogels achieved a maximum conductivity of 1236 S m. The highest EMI SE of the hybrid aerogels was up to 86.9 dB at 12.4 GHz for the 2 mm sample, while the SSE/t reached up to 25 078.1 dB cm^2 g^{-1} for the 1 mm sample, which can be attributed to the well-constructed 3D lamellar conductive network after hybridizing the MXene with graphene in the aerogels. The results show great enhancement compared with the previously reported work on anisotropic MXene/graphene hybrid aerogels and our previous work.

Results and discussion

Fig. 1 illustrates the schematics of the 3D printing MXene/graphene hybrid aerogels processes. At first, MXene and graphene oxide (GO) sheets were dispersed into TBA (*tert*-butyl alcohol) aqueous solutions to prepare the MXene/GO mixed dispersions. Three kinds of mixed dispersions with MXene/GO concentration ratios of 1 : 3, 2 : 3 and 3 : 3 were prepared and labeled as MGO-1, MGO-2 and MGO-3, respectively. Then, one of the three GO dispersions was extruded by the customized extrusion head on a cryogenic substrate. Finally, after freeze-drying and chemical reduction, the lamellar MXene/graphene hybrid aerogel was prepared. There are three key points of the proposed 3D printing method. (1) The slit extrusion heads should be designed according to the rheological property of each dispersion. Then, the corresponding dispersions were extruded to form long-range ordered liquid crystals. (2) The addition of 40 wt% TBA can restrict the size of the ice growth and maintain the extruded liquid crystal orientation as much as possible when the dispersions were extruded on the cryogenic substrate. (3) The chemical reduction process can not only reduce graphene oxide, but also cause the neighbor sheets to be assembled more tightly by liquid capillary force, which will make the final lamellar aerogel structure more ordered. Based on these points, the MXene addition influence mechanism on the structural and electrical properties should be carefully studied.

The hybrid aerogels prepared by these three kinds of dispersions were named as MGA-1, MGA-2 and MGA-3, respectively. As a control group, pure GO dispersion and the corresponding graphene aerogels without the MXene were also prepared by the same processes, named as MGO-0 and MGA-0, respectively. It should be noted that the GO concentrations were kept the same at 0.3 wt% in all four kinds of dispersions.

The rheological properties of the three kinds of MXene/GO mixed dispersions and pure GO dispersion are presented in Fig. 2. The relationship between the shear viscosity and shear rate of the four kinds of dispersions are shown in Fig. 2a. It can be observed that with the shear rate increasing from 0.1 s^{-1} to 1000 s^{-1}, the shear viscosities of the four kinds of dispersions decreased monotonically and rapidly with almost the same trend. This means that all of the dispersions show typical shear

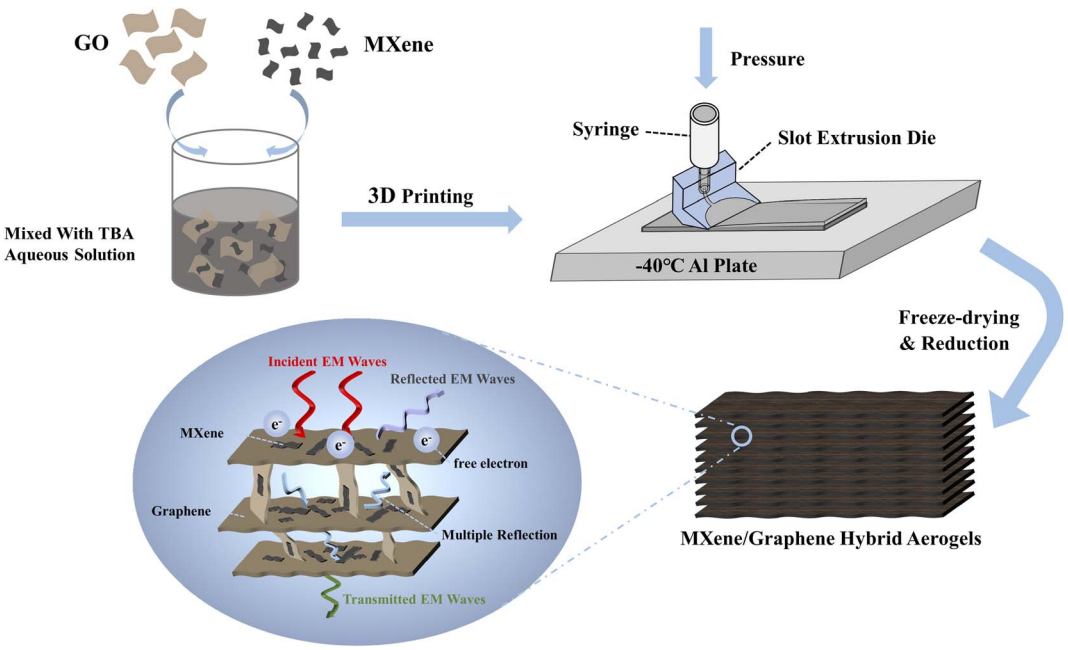

Fig. 1 Schematics of the 3D printing MXene/graphene hybrid aerogels processes. The conceived EMI shielding mechanism of the hybrid lamellar aerogels is presented in the oval inset.

Open Access Article. Published on 01 September 2022. Downloaded on 4/29/2026 2:23:41 AM.
This article is licensed under a Creative Commons Attribution-NonCommercial 3.0 Unported Licence.

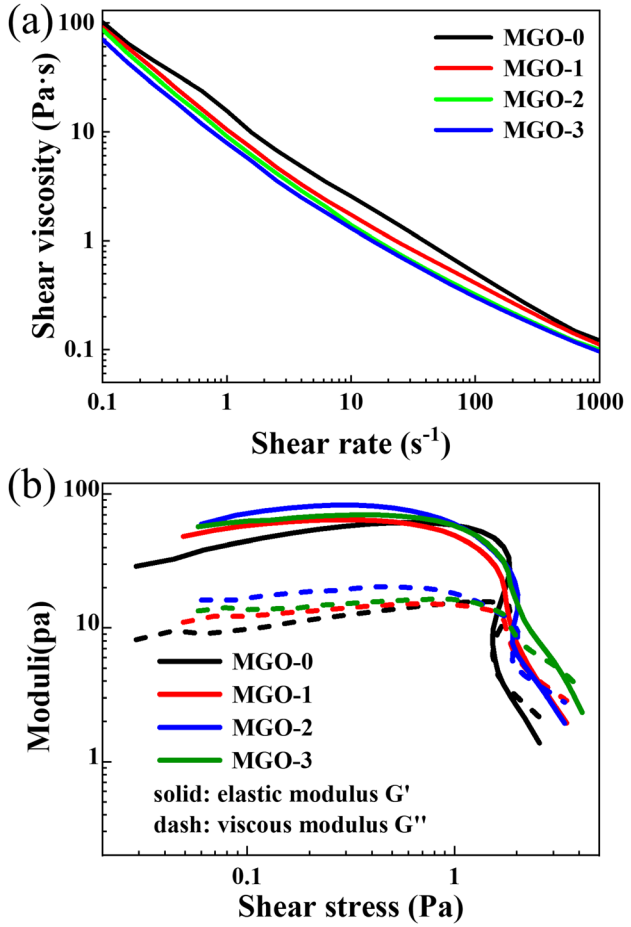

Fig. 2 Rheological properties of the three kinds of MXene/GO mixed dispersions and pure GO dispersion. (a) Shear viscosity as a function of the shear rate; (b) elastic (G') and viscous (G'') moduli as a function of the shear stress.

thinning phenomenon, which is due to the distributions of MXene and GO sheets in the dispersions turning from disordered to highly ordered with the sheet orientation parallel to the direction of the shear force. Meanwhile, with the increase in the MXene concentration, the shear viscosities of the four kinds of dispersions generally showed slight decreases at the same shear rate. It can be deduced that since the MXene sheet size is much smaller than that of GO, the addition of MXene shows a slight lubrication effect between the GO sheets when the dispersions bear the shear force, while also slightly contributing to the decrease in the viscosity. In Fig. 2b, there are clear turning points in all of the curves. On the left side of the turning points, the elastic moduli (G') are higher than the viscous moduli (G'') of all of the dispersions. It should be noted that the addition of MXene slightly influences the G' and G'' but not monotonically. This is probably due to the big size difference between the MXene and GO sheets. The MXene sheets tend to fill the spaces between the GO sheets in the mixed dispersions. When the amount of MXene is low enough, the addition of MXene will increase the G' and G'' of the dispersions; when the amount of MXene is too high, the spaces between the GO sheets will be nearly fully filled, and the G' and G'' of the dispersions will decrease with the addition of MXene. On the right side of the turning points, the G' and G'' of all of the dispersions decrease rapidly. This indicates that when passing through the flow channel, the sheets under high shear stress will turn into an oriented distribution. Meanwhile, the speed of decrease in G' and G'' of the dispersions with a large amount of MXene is slower than that with a lower amount of MXene. This is also related to the MXene filling degree between the GO sheets.

Fig. 3 shows the SEM images of the hybrid aerogels printed by the four kinds of dispersions after freeze-drying and reduction. It can be observed in Fig. 3a–d that all of the samples exhibit lamellar structures, which originated from the shear force on the dispersions by the customized extrusion heads. In Fig. 3a, the lamellar structure of MGA-0 is composed of the lateral-oriented and close-assembled sheets (LCN) layers and the many small cellular structures between them. In general, the LCN layers are not clearly separated from each other. In Fig. 3b, the lamellar structure of MGA-1 becomes more distinguishable than that of MGA-0 since the cellular structures between the LCN layers become larger. In Fig. 3c, compared with MGA-1, the LCN layers of MGA-2 become thicker, and the amount of cellular structures are reduced. This makes the lamellar structure of MGA-2 clearer than that of MGA-1. In Fig. 3d, the LCN layers of MGA-3 continue to become thicker than that of MGA-2, and the distances between the LCN layers become very large to a value of about 10–15 μm. This makes the definition of the layered structure very clear. There are almost no cellular structures in MGA-3, and some thin and close-assembled sheets play the role of bridges to connect the neighboring LCN layers. From the SEM images in Fig. 3, it can be deduced that there is a competition mechanism in the structure formation process. Because reduced graphene oxide sheets provide hydrophobic surfaces after chemical reduction, whereas MXene sheets have hydrophilic surfaces, the increasing amount of the small size MXene sheets will introduce more capillary bridges with large capillary force between the large size graphene sheets. This will increase the possibility of the close-assembly of sheets after chemical reduction. Since MXene is less flexible than graphene, a greater amount of the MXene sheets closely assembled with graphene will make the LCN layers more rigid. Therefore, the LCN layers in MGA-3 are flat and separated with large distances. Such kind of structure will be very suitable for the enhancement of EMI SE. The corresponding elemental mapping of C, O, Ti and F for MGA-3 exhibit the lamellar distribution following the LCN layers. It should be noted that the distribution boundary of Ti is blurry, which indicates that there are some MXene sheets that are not closely assembled and spreading in the space between the LCN layers. The existence of O indicates that there are some GO sheets not being reduced. It should also be noted that the brightness of the elemental mapping of F was increased for easy distinguishing, and the original mapping of F is illustrated in Fig. S1.†

Fig. 4a shows the densities of the four kinds of aerogels. It should be noted that the density calculation errors introduced by the volume measurement are presented by the error bars in Fig. 4a. The density of MGA-0 is 10.8 mg cm^{-3}. The densities of

© 2022 The Author(s). Published by the Royal Society of Chemistry

Open Access Article. Published on 01 September 2022. Downloaded on 4/29/2026 2:23:41 AM.
This article is licensed under a Creative Commons Attribution-NonCommercial 3.0 Unported Licence.

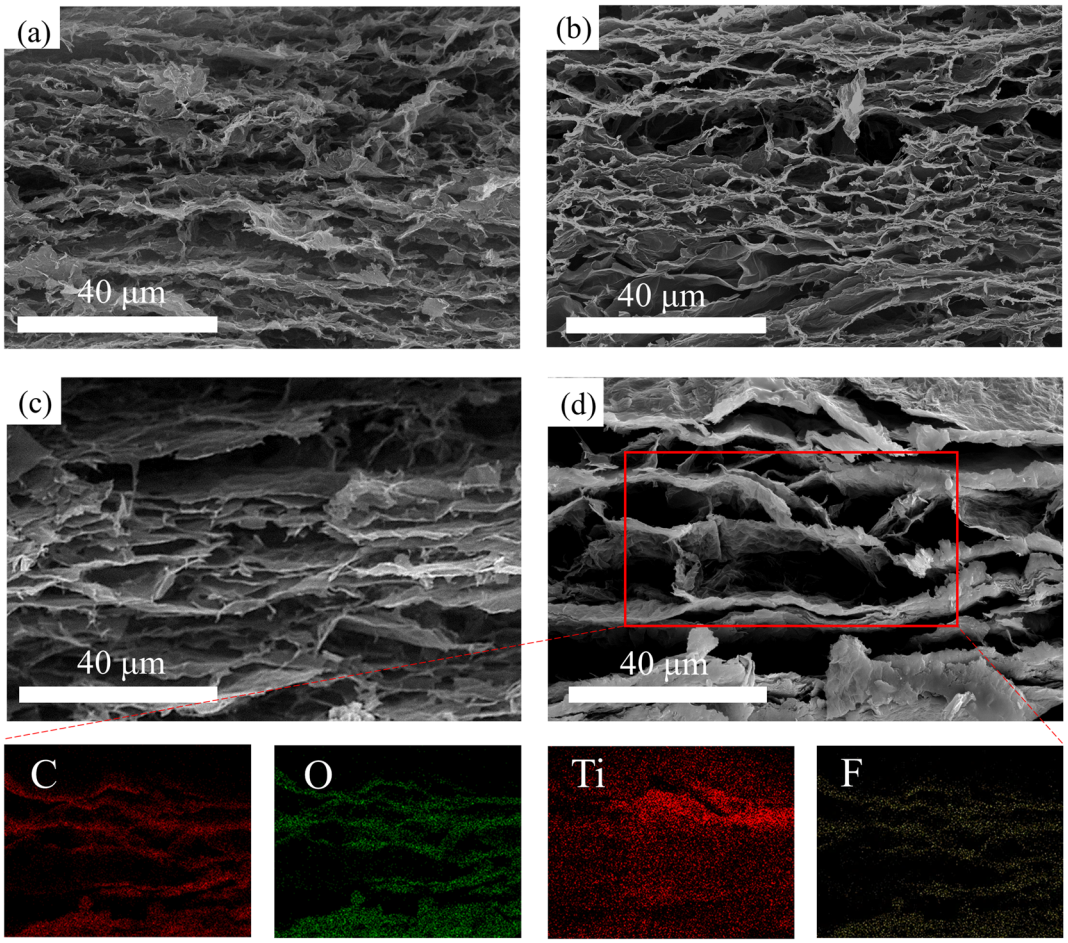

Fig. 3 Scanning electron microscopy (SEM) image of (a) MGA-0, (b) MGA-1, (c) MGA-2, (d) MGA-3, and corresponding EDX elemental mappings of C, O, Ti and F in the region of the red frame for MGA-3.

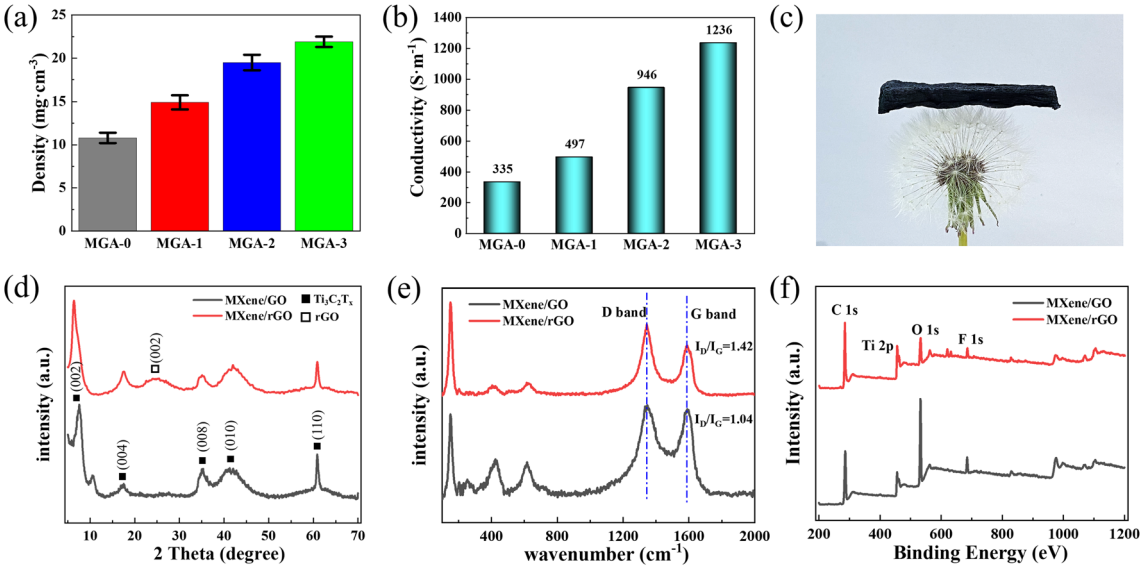

Fig. 4 (a) Densities and (b) electrical conductivities of MGA-0, MGA-1, MGA-2 and MGA-3. (c) Photograph of MGA-3 on a dandelion. Structure properties of MGA-3 before (black) and after reduction (red) measured by (d) X-ray diffraction (XRD) patterns, (e) Raman spectroscopy, and (f) X-ray photoelectron spectroscopy (XPS).

Open Access Article. Published on 01 September 2022. Downloaded on 4/29/2026 2:23:41 AM.
This article is licensed under a Creative Commons Attribution-NonCommercial 3.0 Unported Licence.

MXene/graphene hybrid aerogels increased from 14.9 mg cm^{-3} (MGA-1) to 19.5 mg cm^{-3} (MGA-2), and then to 21.9 mg cm^{-3} (MGA-3) with the increasing MXene concentration in the dispersions. It should be noted that the density difference between MGA-3 and MGA-2 (2.4 mg cm^{-3}) is much smaller than that between MGA-2 and MGA-1 (4.6 mg cm^{-3}), as well as between MGA-1 and MGA-0 (4.1 mg cm^{-3}). This indicates that there is a saturation amount of MXene sheets to be hybridized into the MXene/graphene hybrid aerogels. When the ratio of MXene in the dispersion is larger than the saturation value, the redundant MXene sheets will be washed after reduction. The conductivities of the four kinds of aerogels are shown in Fig. 4b. When only 0.1 wt% MXene in the dispersion was added, the conductivity increased from 335 S m^{-1} for MGA-0 to 497 S m^{-1} for MGA-1. Upon continuing to increase the MXene concentration by 0.1 wt%, more MXene sheets were hybridized into the aerogels, and the conductivities of the MXene/graphene hybrid aerogels increased from 497 S m^{-1} for MGA-1 to 946 S m^{-1} for MGA-2, then to 1236 S m^{-1} for MGA-3. The conductivity of MGA-3 is about 3.69 times that of MGA-0, which demonstrates the successful hybridization of MXene and graphene sheets by 3D printing.

Fig. 4c is a photograph of the MGA-3 sample placed on a dandelion, which exhibits its ultralight property. It should be noted that after freeze-drying and chemical reduction, the sample surface undulates. Fig. 4d shows the X-ray diffraction (XRD) patterns of the MGA-3 sample before and after reduction. Before reduction, there is a (001) diffraction peak of GO at 10.6° that can be observed. After reduction, the (001) peak disappeared, and a new (002) peak of graphene at 25.3° emerged, which indicates that most of the GO sheets were reduced. The broad range of the graphene (002) peak is a result of the combination of different spacings between the graphene sheets. It can be observed that the (002) sharp peak of $Ti_3C_2T_x$ shifts from $2\theta = 7.6°$ before reduction to 6.5° after reduction, which indicates that the d-spacing of the sheets changes from 11.6 Å to 13.2 Å. The other diffraction peaks at $2\theta = 17.4°$, 35.4°, 42.1° and 60.8° correspond to the (004), (008), (010) and (110) planes of $Ti_3C_2T_x$,[21] respectively. Meanwhile, the XRD of the pure Mxene aerogels and small angle X-ray scattering (SAXS) patterns of the Mxene/rGO aerogels can be seen in Fig. S5 and S6.† Fig. 4e illustrates the Raman spectra of MGA-3 before and after reduction. Two typical scattering peaks related to the reduction effect at 1345 cm^{-1} (D-band) and 1591 cm^{-1} (G-band) are observed in Fig. 4e, which are considered as evidence for the existence of graphene. The D-band represents structural defects or functional additives in GO, and the G-band represents the in-plane vibration of the sp^2 carbon atoms.[27] Therefore, the intensity ratio (I_D/I_G) was calculated to illustrate the reduction level of GO.[28] Compared with the I_D/I_G ratio of 1.04 for MGA-3 before reduction, MGA-3 has a higher value of 1.42, which proves that most of the oxygen-containing functional groups were removed from the carbon skeleton. The main characteristic peaks of $Ti_3C_2T_x$ were also identified. The sharp peak at 150.3 cm^{-1} is attributed to titanium dioxide, which is caused by the inevitable oxidation of $Ti_3C_2T_x$. The wide peaks at 253.2 cm^{-1} and 418.9 cm^{-1} represent the in-plane vibrations of the O–H surface groups attached to titanium atoms.[22] The wide peak at 618.4 cm^{-1} is assigned to the Ti–C vibrations. Fig. 4f illustrates the X-ray photoelectron spectroscopy (XPS) results of the surface chemical compositions of the MGA-3 sample before and after reduction. There are four main elements in Fig. 4f, namely carbon, titanium, oxygen and fluorine, which terminated on the surface of the aerogels. It can be observed that after reduction, the intensity of the C 1s peak at around 285.1 eV shows clear enhancement, while the intensity of the O 1s peak at around 532.1 eV appears to have a large decrease. This also means that most of the GO sheets were reduced. In detail, as shown in Fig. S4a,† the Ti 2p peak regions of the MGA-3 are mainly composed of the peaks at 455.1 eV (corresponding to the Ti–C bond), 455.6 and 461.5 eV (corresponding to the Ti(II) bond), 456.5 and 463.1 eV (corresponding to the Ti(III) bond), and 459.3 eV (corresponding to the Ti–O bond).[23] In Fig. S4b,† the high-resolution C 1s spectrum of MGA-3 further demonstrates the existence of the C–Ti–O/F (282.2 eV), C–C (284.7 eV), C–O (285.4 eV) and C=O (289.1 eV) bonds.[24] In addition, the XPS spectrum of MGA-3 shows the presence of terminal fluorine, hydroxyl groups and oxygen-containing functional groups on the aerogel surface, which can act as local dipoles when subjected to an alternating electromagnetic field. Polarization losses will be generated by these local dipoles after interaction with an electromagnetic wave to improve the EMI shielding performance.[10]

Fig. 5a shows the EMI SE in the X-bands of MGA-0, MGA-1, MGA-2, and MGA-3 with the thickness of 2 mm. It can be observed that the EMI SE of MGA-0 is nearly independent of the electromagnetic wave frequency, and the average value in the X-band is at a low level of about 21 dB. With the addition of MXene, the average EMI SE values in the X-band of the hybrid aerogels increase from 36.9 dB for MGA-1 to 62.5 dB for MGA-2, and then to 78.5 dB for MGA-3. The maximum EMI SE achieves up to 86.9 dB for MGA-3 at 12.4 GHz. It should be noted that the EMI SE of each hybrid aerogel increases with the electromagnetic wave frequency, and the increasing speed becomes faster from MGA-1 to MGA-2, then to MGA-3, which is mainly due to the increase of the electrical conductivity with the addition of MXene.

Fig. 5b shows the thickness-dependent EMI SE of MGA-3. The EMI SE shows a continuous enhancement with increasing thickness. Except for the 2 mm sample mentioned above, the average EMI SE values are 53.5 dB and 68.5 dB for the 1 mm and 1.5 mm samples, respectively. Fig. 5c shows the absorption shielding effectiveness (SE_A), reflective shielding effectiveness (SE_R) and total shielding effectiveness (SE_{Total}) of the four kinds of aerogels at 10.2 GHz. As expected, the SE_A is much higher than SE_R for all aerogels. It indicates that the electromagnetic waves are mainly absorbed during the multi-reflection between the lamellar layers after penetrating the aerogels. In detail, the percentage of SE_A in SE_{Total} are 87.6% for MGA-0, 92.8% for MGA-1, 94% for MGA-2, and 94.5% for MGA-3, which indicates that the addition of MXene can significantly increase the absorption of electromagnetic waves by increasing the conductivity. It should be noted that with the increase of the MXene content, SE_R increases from 2.59 dB for MGA-0 to 2.61

© 2022 The Author(s). Published by the Royal Society of Chemistry

Open Access Article. Published on 01 September 2022. Downloaded on 4/29/2026 2:23:41 AM.
This article is licensed under a Creative Commons Attribution-NonCommercial 3.0 Unported Licence.

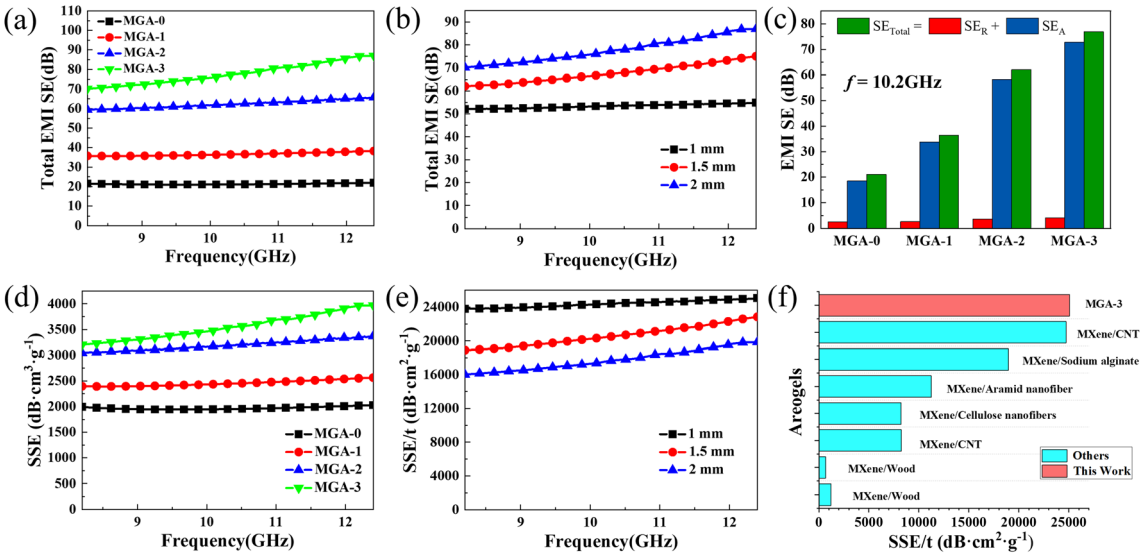

Fig. 5 (a) EMI SE in the X-band of MGA-0, MGA-1, MGA-2 and MGA-3 with the thickness of 2 mm. (b) EMI SE in the X-band of MGA-3 with the thickness from 1 mm to 2 mm. (c) Contrast of the total shielding effectiveness (SE_{Total}), absorption shielding effectiveness (SE_A), and reflective shielding effectiveness (SE_R) at 10.2 GHz of MGA-0, MGA-1, MGA-2 and MGA-3 with the thickness of 2 mm. (d) SSE of MGA-0, MGA-1, MGA-2 and MGA-3 with the thickness of 2 mm. (e) SSE/*t* of MGA-3 with the thickness from 1 mm to 2 mm. (f) SSE/*t* value comparison between this work and the reported MXene-based anisotropic nanocomposite aerogels.

dB for MGA-1, then to 3.7 dB for MGA-2, then to 4.2 dB for MGA-3. The small increases of SE_R may be attributed to the increase of the impedance mismatch between the aerogel surface and the free space. Fig. 5d shows the specific shielding effectiveness (SSE, defined as EMI SE divided by density) of the four kinds of aerogels. MGA-3 exhibits the highest SSE curve ranging from 3205.6 dB cm^3 g^{-1} to 3970.9 dB cm^3 g^{-1}. Fig. 5e shows the absolute shielding effectiveness (SSE/*t*, defined as SSE divided by thickness) of MGA-3 with different thicknesses. The SSE/*t* appears to be inversely dependent on the thickness. The 1 mm sample exhibits the highest curve, with the maximum SSE/*t* achieving 25 078.1 dB cm^2 g^{-1} at 12.4 GHz. The maximum SSE/*t* value of this work is compared with those of other reported MXene-based anisotropic nanocomposite aerogels in Fig. 5f. It can be found that the SSE/*t* of 1 mm MGA-3 is very high compared with those of other MXene-based anisotropic nanocomposite aerogels.[2,19,24–28] This can be attributed to the EMI shielding mechanism of the MXene/graphene hybrid aerogels with 3D lamellar structure. As shown in the oval inset in Fig. 1, when the incident electromagnetic waves enter the aerogel surface perpendicularly, a small part of the electromagnetic waves will be reflected due to the impedance mismatch. Then, the rest of the electromagnetic waves will enter the inside layers. The inside 3D lamellar structure and the large surface area will lead to multiple internal reflection and scattering of the electromagnetic waves in the aerogel, resulting in ohmic loss and a significant drop in the energy.[13,18,29] This is consistent with the results in Fig. 5c, the SE_A is much higher than SE_R. In addition, the rich surface functional groups of MXene as shown in Fig. 4f will cause a polarization of the dipole and interface, which will increase the polarization loss and further improve the attenuation of the electromagnetic waves.[30,31]

Experimental

Materials

The graphene oxide (GO) water dispersion was purchased from Chengdu Institute of Organic Chemistry, Chinese Academy of Science. The $Ti_3C_2T_x$ MXene monolayer water dispersion was purchased from Nanjing/Jiangsu XFNANO Materials Tech Co., Ltd. *Tert*-butyl alcohol (TBA), HI and acetic acid were purchased from Sinopharm Chemical Reagent Co., Ltd.

Preparation and rheological property test of MXene/GO mixed dispersions

The concentration of the purchased $Ti_3C_2T_x$ MXene dispersion is 5 mg mL^{-1}, and the average transverse size is 1–5 μm. The concentration of the GO dispersion is 10 mg mL^{-1}, and the average transverse size is about 50 μm. In order to get the concentrated MXene dispersion, the MXene water dispersion was centrifuged at 10 000 rpm for 2 hours until most of the MXene sheets were precipitated. After that, half of the supernatants were removed, and the remaining MXene dispersion was sonicated for 30 min. The concentrated MXene dispersion (10 mg mL^{-1}) was mixed with the GO dispersion (10 mg mL^{-1}) in the mass ratios of 0 : 3, 1 : 3, 2 : 3 and 1 : 1. Then, *tert*-butyl alcohol (TBA) was added to the mixed dispersions until its concentration reached 40 wt%, stirring for 30 min to obtain the MXene/GO ink for printing, which were labeled as MGO-0, MGO-1, MGO-2 and MGO-3 for the mass ratios of 0 : 3, 1 : 3, 2 : 3 and 3 : 3, respectively. A rheometer (Netzsch instruments, kinexus lab+) was used to study the rheological properties of the four kinds of dispersions. The measurement fixture adopted a conical spindle (angle: 2°, diameter: 40 mm). The air compressor was opened and it was ensured that the pressure in

Open Access Article. Published on 01 September 2022. Downloaded on 4/29/2026 2:23:41 AM. This article is licensed under a Creative Commons Attribution-NonCommercial 3.0 Unported Licence.

the rheometer air bearing reached 3 bar. After inertial calibration and background calibration, about 1.3 mL MXene/GO mixed dispersion was dripped on the sample table. The shear stress and viscosity of two complete (rising and falling) cycles were measured at shear rates between 0.1 and 1000 s^{-1}. Reloading the sample, the elastic and viscous moduli were measured at shear stresses between 0.02 and 5 Pa.

Preparation of lamellar MXene/GO hybrid aerogels

The modified dispenser used for 3D printing was equipped with a five-axis displacement table, which was composed of a three-axis displacement table, a rotary displacement table and an angular displacement table. The aluminum plate was used as the print platform, and its temperature was maintained at −40 °C through the circulating cooling of an ethanol freezing tube. Slit extrusion heads were designed by the rheological properties of the mixed dispersions, which have slit widths of 50 μm.[20] The slit extrusion heads were prepared by a projection micro-stereolithography 3D printer (NanoArch S140, BMF Precision Tech Inc.). After the printed frozen blocks reached the required thickness, the printed samples were freeze-dried in the lyophilizer (Scientz-12, Ningbo Scientz Biotechnology Co., Ltd) for 24 hours (the air pressure is lower than 5 Pa). Next, the acid mixtures of HI : HAC = 1 : 2 were used for chemical reduction of the samples in a beaker at 40 °C for 24 hours. The reduced aerogels were then cleaned repeatedly with 40 wt% TBA aqueous solution to remove the residual acid in the samples. In order to avoid the curling of aerogels caused by liquid surface tension during freeze-drying, the samples were soaked in TBA and frozen for 2 h. MXene/graphene aerogels (MGAs) were prepared after freeze-drying for 24 h. According to the mass fraction of TBA in the printed MXene/graphene dispersions, the aerogels were named as MGA-0, MGA-1, MGA-2 and MGA-3, respectively.

Characterization

A NETZSCH instruments, Kinexus lab+ rheometer was used to measure the rheological properties of the MXene/GO dispersions. The morphology and EDX element spectra of the hybrid aerogels were measured by an FEI Quanta FEG 250 scanning electron microscope (SEM). The microstructures of the aerogels were measured by a Horiba-JY, LABRAM HR Raman spectrometer. The X-ray diffraction (XRD) patterns of the samples were measured by a Bruker AXS GmbH, D8 Advance X-ray diffractometer. A Thermo Fisher Scientific, Escalab 250Xi X-ray photoelectron spectroscope (XPS) was used to measure the chemical bonding structures of the samples. The masses of the aerogels were measured by a Shanghai Sunny Hengping Scientific Instrument Co., Ltd, FA2140 analytical balance. The densities of the aerogels were calculated by dividing the mass by the corresponding volume. A Suzhou Jingge Electronic Co. Ltd, ST-2258A four probe resistivity meter was used to measure the conductivities of the samples. A Keysight N5222A vector network analyzer was used to measure the electromagnetic interference shielding effectiveness (EMI SE) in the X-band range of 8.2 to 12.4 GHz for the aerogels.

Conclusions

We fabricated lamellar $Ti_3C_2T_x$ MXene/graphene aerogels with enhanced electromagnetic shielding properties by 3D printing. MXene sheets were successfully hybridized with graphene, which significantly improved the conductivities of the hybrid aerogels. In addition, there were many terminal functional groups on the surface of MXene sheets, which was conducive to the rapid attenuation of the electromagnetic waves. The average EMI SE of the MGA-3 in the X-band reached 76.9 dB with a maximum value of 86.9 dB, while the SSE/t of MGA-3 with the thickness of 1 mm achieved up to 25 078.1 dB cm^2 g^{-1}. This is higher than the values of most of the reported MXene-based anisotropic nanocomposite aerogels. It is worth noting that other 2D material-based aerogels can also be prepared by the 3D printing method reported in this paper, and many functional nanoparticles can be hybridized into the 3D lamellar frameworks, which will expand the applications of 2D materials in the fields of electromagnetic shielding, supercapacitors and sensors.

Conflicts of interest

There are no conflicts to declare.

Acknowledgements

The authors gratefully acknowledge financial support by the National Natural Science Foundation of China (No. 61575216), Key R&D programs in Jiangsu (No. BE2017082), R&D Plan for Key Areas of Guangdong Province (No. 2018B090905002), Suzhou Science and Technology Program (No. SYG201850), and Fundamental Research Funds for the Central Universities (No. WK5290000002).

Notes and references

1 L. Liang, Q. Li, X. Yan, Y. Feng, Y. Wang, H.-B. Zhang, X. Zhou, C. Liu, C. Shen and X. Xie, *ACS Nano*, 2021, **15**, 6622–6632.
2 P. Sambyal, A. Iqbal, J. Hong, H. Kim, M.-K. Kim, S. M. Hong, M. Han, Y. Gogotsi and C. M. Koo, *ACS Appl. Mater. Interfaces*, 2019, **11**, 38046–38054.
3 L. Kheifets, A. Afifi Abdelmonem and R. Shimkhada, *Environ. Health Perspect.*, 2006, **114**, 1532–1537.
4 S. Wu, M. Zou, Z. Li, D. Chen, H. Zhang, Y. Yuan, Y. Pei and A. Cao, *Small*, 2018, **14**, 1800634.
5 J. Ma, K. Wang and M. Zhan, *RSC Adv.*, 2015, **5**, 65283–65296.
6 K. Ji, H. Zhao, J. Zhang, J. Chen and Z. Dai, *Appl. Surf. Sci.*, 2014, **311**, 351–356.
7 N. C. Das, Y. Liu, K. Yang, W. Peng, S. Maiti and H. Wang, *Polym. Eng. Sci.*, 2009, **49**, 1627–1634.
8 D. D. L. Chung, *Carbon*, 2001, **39**, 279–285.
9 Z.-H. Zhou, M.-Z. Li, H.-D. Huang, L. Li, B. Yang, D.-X. Yan and Z.-M. Li, *ACS Appl. Mater. Interfaces*, 2020, **12**, 18840–18849.

© 2022 The Author(s). Published by the Royal Society of Chemistry

Open Access Article. Published on 01 September 2022. Downloaded on 4/29/2026 2:23:41 AM.
This article is licensed under a Creative Commons Attribution-NonCommercial 3.0 Unported Licence.

10 F. Shahzad, M. Alhabeb, B. Hatter Christine, B. Anasori, S. Man Hong, M. Koo Chong and Y. Gogotsi, *Science*, 2016, **353**, 1137–1140.
11 R. Bian, G. He, W. Zhi, S. Xiang, T. Wang and D. Cai, *J. Mater. Chem. C*, 2019, **7**, 474–478.
12 M. Naguib, M. Kurtoglu, V. Presser, J. Lu, J. Niu, M. Heon, L. Hultman, Y. Gogotsi and M. W. Barsoum, *Adv. Mater.*, 2011, **23**, 4248–4253.
13 Z. Fan, D. Wang, Y. Yuan, Y. Wang, Z. Cheng, Y. Liu and Z. Xie, *Chem. Eng. J.*, 2020, **381**, 122696.
14 G.-M. Weng, J. Li, M. Alhabeb, C. Karpovich, H. Wang, J. Lipton, K. Maleski, J. Kong, E. Shaulsky, M. Elimelech, Y. Gogotsi and A. D. Taylor, *Adv. Funct. Mater.*, 2018, **28**, 1803360.
15 M. Alhabeb, K. Maleski, B. Anasori, P. Lelyukh, L. Clark, S. Sin and Y. Gogotsi, *Chem. Mater.*, 2017, **29**, 7633–7644.
16 W.-T. Cao, F.-F. Chen, Y.-J. Zhu, Y.-G. Zhang, Y.-Y. Jiang, M.-G. Ma and F. Chen, *ACS Nano*, 2018, **12**, 4583–4593.
17 C. J. Zhang, S. Pinilla, N. McEyoy, C. P. Cullen, B. Anasori, E. Long, S.-H. Park, A. Seral-Ascaso, A. Shmeliov, D. Krishnan, C. Morant, X. Liu, G. S. Duesberg, Y. Gogotsi and V. Nicolosi, *Chem. Mater.*, 2017, **29**, 4848–4856.
18 S. Zhao, H.-B. Zhang, J.-Q. Luo, Q.-W. Wang, B. Xu, S. Hong and Z.-Z. Yu, *ACS Nano*, 2018, **12**, 11193–11202.
19 C. Liang, H. Qiu, P. Song, X. Shi, J. Kong and J. Gu, *Sci. Bull.*, 2020, **65**, 616–622.
20 H. Guo, T. Hua, J. Qin, Q. Wu, R. Wang, B. Qian, L. Li and X. Shi, *Adv. Mater. Technol.*, 2022, 2101699.
21 L. Wang, H. Liu, X. Lv, G. Cui and G. Gu, *J. Alloys Compd.*, 2020, **828**, 154251.
22 A. Sarycheva and Y. Gogotsi, *Chem. Mater.*, 2020, **32**, 3480–3488.
23 J. Song, X. Guo, J. Zhang, Y. Chen, C. Zhang, L. Luo, F. Wang and G. Wang, *J. Mater. Chem. A*, 2019, **7**, 6507–6513.
24 M. Zhu, X. Yan, H. Xu, Y. Xu and L. Kong, *Carbon*, 2021, **182**, 806–814.
25 X. Wu, B. Han, H.-B. Zhang, X. Xie, T. Tu, Y. Zhang, Y. Dai, R. Yang and Z.-Z. Yu, *Chem. Eng. J.*, 2020, **381**, 122622.
26 Z. Deng, P. Tang, X. Wu, H.-B. Zhang and Z.-Z. Yu, *ACS Appl. Mater. Interfaces*, 2021, **13**, 20539–20547.
27 Y. Du, J. Xu, J. Fang, Y. Zhang, X. Liu, P. Zuo and Q. Zhuang, *J. Mater. Chem. A*, 2022, **10**, 6690–6700.
28 L. Wang, P. Song, C.-T. Lin, J. Kong and J. Gu, *Research*, 2020, **2020**, 4093732.
29 M. H. Al-Saleh, W. H. Saadeh and U. Sundararaj, *Carbon*, 2013, **60**, 146–156.
30 Y. Lu, S. Zhang, M. He, L. Wei, Y. Chen and R. Liu, *Carbon*, 2021, **178**, 413–435.
31 J. Zhu, H. Gu, Z. Luo, N. Haldolaarachige, D. P. Young, S. Wei and Z. Guo, *Langmuir*, 2012, **28**, 10246–10255.

© 2022 The Author(s). Published by the Royal Society of Chemistry